ACS APPLIED MATERIALS & INTERFACES

Forum Article

www.acsami.org

Patterned Diblock Co-Polymer Thin Films as Templates for Advanced Anisotropic Metal Nanostructures

Stephan V. Roth,*[,†] Gonzalo Santoro,[†] Johannes F. H. Risch,[†] Shun Yu,[†,#] Matthias Schwartzkopf,[†] Torsten Boese,[†] Ralph Döhrmann,[†] Peng Zhang,[†] Bastian Besner,[‡] Philipp Bremer,[‡] Dieter Rukser,[‡] Michael A. Rübhausen,[‡] Nick J. Terrill,[§] Paul A. Staniec,[§] Yuan Yao,[⊥] Ezzeldin Metwalli,[⊥] and Peter Müller-Buschbaum[⊥]

[†]Deutsches Elektronen-Synchrotron (DESY), Notkestrasse 85, D-22607 Hamburg, Germany

[‡]Institut für Nanostruktur- und Festkörperforschung, Center for Free-Electron Laser Science, Advanced Study Group−APOG, University of Hamburg, Luruper Chaussee 149, 22761 D Hamburg, Germany

[§]Diamond Light Source, Harwell Science and Innovation Campus, Didcot, Oxfordshire OX11 0QX, United Kingdom

[⊥]Lehrstuhl für Funktionelle Materialien, TU München, James-Franck-Strasse 1, D-85748 Garching, Germany

Supporting Information

ABSTRACT: We demonstrate glancing-angle deposition of gold on a nanostructured diblock copolymer, namely polystyrene-*block*-poly(methyl methacrylate) thin film. Exploiting the selective wetting of gold on the polystyrene block, we are able to fabricate directional hierarchical structures. We prove the asymmetric growth of the gold nanoparticles and are able to extract the different growth laws by in situ scattering methods. The optical anisotropy of these hierarchical hybrid materials is further probed by angular resolved spectroscopic methods. This approach enables us to tailor functional hierarchical layers in nanodevices, such as nanoantennae arrays, organic photovoltaics, and sensor electronics.

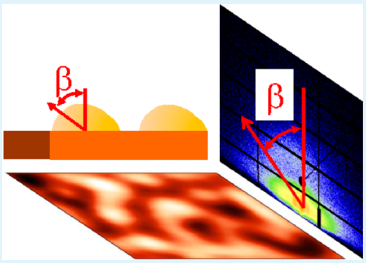

KEYWORDS: *hierarchical materials, grazing incidence scattering, diblock copolymer thin films, nanocomposites, glancing angle deposition*

1. INTRODUCTION

The tailoring of metal nanoparticles layers[1] and hybrid materials plays a crucial role in modern advanced material science.[2−4] The demand ranges from hydrophobic surfaces and [5] flexible sensors[6,7] to organic photovoltaics (OPV)[8,9] and magnetic storage media.[10] The related objective is to combine the tunable nanostructure of diblock copolymeric materials[11,12] with the selective interaction of metals with different polymer materials.[13−15]

The applications of metallic layers cover catalytically active layers[16] via colloidal contacts[17] or nanostructures for sensor applications[6,18] and single electron devices.[19] Often, spray deposition[17,20] and vacuum deposition methods such as molecular beam epitaxy,[21] vapor deposition,[22,23] and sputter deposition[24,25] are employed to achieve the installation of the metallic layer. Normal incidence sputter deposition, i.e., deposition direction normal to the substrate, allows for installing radially symmetric nanoparticles, a process used for SERS[18] and catalysis.[26−28] In contrast, for sensor applications as well as catalysis, the size and length scale of the nanoparticles is on the order of a few nanometers. For electrical contacts, homogeneous layers well above the percolation threshold are used, whereas for OPVs,[29] well-defined two-dimensional stacks are needed. Often, metal nanoparticles are included to increase the light absorption based on plasmons,[30] where the plasmon frequency depends on the nanoparticles' size.[31] On the other hand, the use of oblique incidence glancing angle deposition (GLAD)[32−34] allows for the creation of very versatile compact and columnar nanostructures with designed porosity,[35,36] an attractive option for tailoring OPVs. Another example is to tailor the refractive index of the metal oxide layer.[37] Finally, three-dimensional structures with tailored material composition can be created.[38] This can be further used to create plasmonic devices.[39] Prospectively, this controlled deposition can even be combined with quantum dots to position plasmonic structures.[40]

In our investigations, we combine oblique angle deposition of gold with diblock copolymer substrates to create hierarchical materials. This approach combines the installation of asymmetric, directional nanoparticles with the selected position because of the different interaction of the gold atoms with the polymeric blocks of the diblock copolymer. Prospectively, this opens up new approaches for combining flexible substrates with nanoantennae arrays[41] in flexible electronics and nanowire

Special Issue: Forum on Polymeric Nanostructures: Recent Advances toward Applications

Received: November 5, 2014
Accepted: January 21, 2015
Published: January 30, 2015

DOI: 10.1021/am507727f
ACS Appl. Mater. Interfaces 2015, 7, 12470−12477

production.[42] Furthermore, GLAD structures are used to tune hydrophobicity,[43] and in view of functional textiles[44] and fibers,[45] columnar structures with application in catalysis and purification on flexible substrates become even more important.[46]

2. EXPERIMENTAL METHODS

We investigate the kinetics of the metal layer growth as well as the different installed morphologies and their wavelength-dependent optical reflectivities.

2.1. Sample Preparation. Two series of polystyrene-*block*-poly(methyl methacrylate) (PS-*b*-PMMA) films with different block ratios were prepared. For the in situ as well for the ex situ experiments, all PS-*b*-PMMA thin films were prepared on silicon substrates. For the in situ experiment, the sample size was approximately 3 × 4 cm^2 to allow for scanning of the sample. For the ex situ experiments with a metal layer thicknesses of δ = 0.4, 0.8, 12, and 120 nm, the sample size was 15 × 15 mm^2. The ex situ sample δ = 3.12 nm had a size of approximately 2 × 4 cm^2.

2.1.1. Silicon Substrate Cleaning. The silicon (Si) substrates (p-doped, (100) orientation, Si-Mat, Kaufering) were cleaned by placing them in an acid bath at 80 °C for 15 min. The acid solution consisted of 130 mL of deionized water (H_2O), 70 mL of hydrogen peroxide (H_2O_2), and 200 mL of sulfuric acid (H_2SO_4). After the 15 min in the bath, the samples were rinsed thoroughly with deionized water and then blow dried with N_2 gas.[47]

2.1.2. Diblock Copolymer Thin Films. The PS-*b*-PMMA films were prepared as follows. We used PS-*b*-PMMA with a molecular weight of 45-*b*-44 kg/mol and polydispersity index (PDI) of 1.12, and additionally PS-*b*-PMMA with a molecular weight of 55-*b*-22 kg/mol and polydispersity index (PDI) of 1.09. The polymers were purchased from Polymer Source Inc. (Canada). Concerning the molecular weight of 45-*b*-44 kg/mol, the diblock copolymer templates were prepared by spin-coating of 12.5 mg/mL PS-*b*-PMMA solution in toluene on the precleaned silicon substrates at 2000 rpm for 30 s. All samples were treated at 120 °C for 3 days to install the phase-separated structure. The film thickness was determined by scratching and atomic force microscopy (AFM) to 60 ± 5 nm Concerning the molecular weight of 55-*b*-22 kg/mol, the sample preparation as well as the sputter deposition results are presented in the Supporting Information.

2.2. Grazing Incidence Small-Angle X-ray Scattering (GISAXS). In situ real time grazing incidence small-angle X-ray scattering (GISAXS)[48] is ideally suited for analyzing progressive layer deposition and nanoparticle formation and growth in hybrid materials.[49−52] The in situ deposition experiment was performed at the beamline I22 of Diamond Light Source (DLS), Didcot, U.K.. The beam was monochromatized using a fixed-exit silicon (111) monochromator and focused via two bimorph mirrors to deliver a beam size of 220 × 70 μm^2 at the sample position. The focused beam was further cleaned using a cross-slit approximately 0.5 m from the sample position. The selected X-ray wavelength was 0.1128 nm. The sample-to-detector distance (SDD) was set to 3775 mm. A two-dimensional detector (Pilatus3 2M, Dectris, Switzerland, number of pixels 1475 × 1679, pixel size 172 × 172 μm^2) was used. The flight path between sputter deposition chamber and detector was evacuated. One beam stop was used to shield the specular reflected beam. The angle of incidence was set to α_i = 0.6°. The direct beam was blocked by a beam stop with a diode. A sketch of the geometry is shown in Figure S2 in the Supporting Information together with a description of the measurement procedure.

2.3. Glancing Angle Deposition (GLAD). The radio frequency (r.f.) sputter deposition chamber was incorporated at the sample position of I22 on a heavy load goniometer (Huber, Germany), allowing for adjustment of *x*/*y*/*z*, tilt (rotation perpendicular to beam) and incident angle. The base pressure was 1.5 × 10^{-6} mbar. The Argon (Ar) pressure was 2.4 × 10^{-2} mbar/2.5 × 10^{-2} mbar (in situ experiment and ex situ samples, respectively). The Au (99.9999% purity, Mateck, Germany) target was water-cooled, and the radio frequency was 13.56 MHz. The distance between target and sample midpoint was 90 mm. The glancing angle was 10° with respect to the sample surface (see Figure 1). The voltage was U = 975 ± 10 V and U = 1190 ± 10 V (in situ experiment and ex situ samples, respectively). The details of the sputter deposition chamber and its routine incorporation in a synchrotron beamline are described elsewhere.[57]

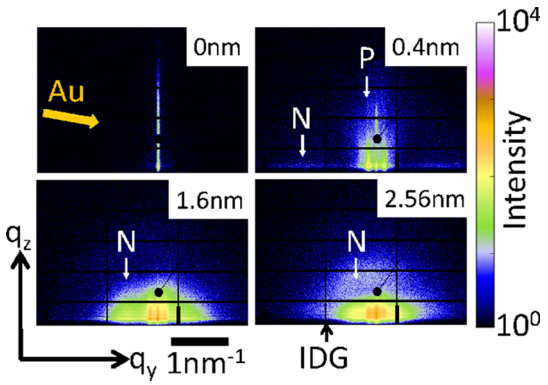

Figure 1. Selected grazing incidence small-angle X-ray scattering (GISAXS) patterns. The color scale is logarithmic. q_y, q_z denote a reciprocal space coordinate system. Au and the orange arrow denote the glancing angle deposition of gold. The arrows denoted N and P correspond to the scattering contribution of the self-assembled Au nanoparticles (N) and the scattering contribution from the diblock copolymer substrate (P). IDG denotes one of the intermodule gaps of the detector. The nominal thickness δ of deposited Au is shown on each pattern. The red arrow denotes the growth direction of the Au nanoparticles under an angle β = 55° ± 3°.

2.4. Real Space Imaging. The real space imaging was performed ex situ after sputter deposition.

2.4.1. Atomic Force Microscopy (AFM). To obtain an overview on the samples and their morphology, we use the NT-MDT Aura system in semicontact mode. A NSG-30 cantilever (NT-MDT, Apeldoorn, The Netherlands) with a spring constant of 40 N/m was used. Samples were probed at ambient conditions, and the measured data were corrected for background and cantilever movement.

2.4.2. Field-Emission Scanning Electron Microscopy (FESEM). The SEM images were taken with an NVision 40 Gemini (Zeiss) field-emission SEM operating at an accelerating voltage of 5 kV and at a low working distance of 3.0 mm.

2.5. Spectroscopy. To investigate the directional response of the installed hierarchical hybrid structure, we used spectroscopic ellipsometry as well as UV−vis spectroscopy.

2.5.1. Spectroscopic Ellipsometry. Spectroscopic ellipsometry measurements were performed over a spectral range of 0.5−4.2 eV in the polarizer−compensator−sample−analyzer (PCSA) configuration using a SE850 Ellipsometer from SENTECH Instruments GmbH. The ellipsometric angles Δ and Ψ were measured with a step width of 20 meV. For a complete characterization of the samples, three different angles of incidence were used, along with a complete rotation of the sample azimuth ω in steps of 12°. As birefringence was expected due to the anisotropic nanostructures, the polarizer and compensator were held at a fixed position. Using lenses, the illuminated area was approximately 1 × 1 mm^2 at the same spot during the rotation. Due to the biaxial layer converting p to s polarized light and s to p polarized light, the ellipsometric angles are no longer an eigenstate of the sample and the measured values depend on the polarization state of the incident light. By rotating the sample, different components of the dielectric tensor are accessed, providing a complete characterization of the sample.

2.5.2. UV−Vis Spectroscopy. Light from a 150 W xenon lamp (LOT-Oriel, Darmstadt, Germany) was focused into a fiber optic cable. After exiting the light cable, the light beam was further focused using lenses (Thorlabs, USA, New Jersey) to a 0.5 × 0.5 mm^2spot size on the sample. The reflected light was collected by a fiber optical cable,

DOI: 10.1021/am507727f
ACS Appl. Mater. Interfaces 2015, 7, 12470−12477

at $\alpha_{inc} = \alpha_f$. The spectrum was analyzed using an Andor Shamrock spectrometer (Belfast, Ireland), equipped with a grid monochromator. A CCD camera cooled to −40 °C was used to record the spectral intensities. A photo of the experimental setup as well as the results is presented in the Supporting Information, along with the results.

3. RESULTS AND DISCUSSION

Figure 1 shows selected GISAXS pattern at Au layer thicknesses of δ = 0, 0.4, 1.6, and 2.56 nm. At δ = 0 nm, a strong intensity distribution along the q_z direction is visible, originating from the correlated roughness of the PS-*b*-PMMA film. The small shoulders at $q_y \approx 0.14$ nm^{-1} stem from the phase separated structure, which is also seen in the AFM images presented in Figure 3a and are discussed later. Upon increased deposition, we note two phenomena. First, the GISAXS-signal from the phase-separated polymer structure increases in intensity, whereas the q_y position of the now strong peaks stays constant. This already indicates a selective growth of the Au nanoparticles on the PS component of the diblock copolymer.[51,54−56] Second, the scattered intensity shows an asymmetry with respect to the q_z axis. The direction of Au deposition under the oblique angle of 10° is indicated in Figure 1. The asymmetric intensity distribution is a fingerprint of the anisotropic growth of the nanoparticles, being directly detected by GISAXS. Using the procedure for extracting the growth angle of the nanostructures outlined in the Supporting Information, we obtain an angle β = 55° ± 3°, in perfect agreement with previous work by Hawkeye et al.[58] This angle is also indicated in Figure 1.

The line-cuts in Figure 2 show the intensity $I(q_y, q_z = 0.72 \pm 0.04$ nm^{-1}, $\delta)$, and thus depict the evolution of the GISAXS

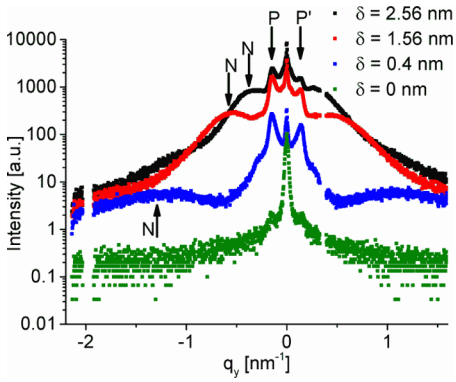

Figure 2. Out-of-plane q_y cuts performed at a fixed $q_z = 0.72 \pm 0.04$ nm^{-1} in the GISAXS pattern from Figure 1 are shown. The nominal thickness of deposited Au is indicated. P, P′ denote the characteristic structure of the diblock copolymer substrate, N that of the Au nanoparticles. Please note the noncentrosymmetric shape of the q_y profiles because of GLAD.

signal stemming from the polymer thin film and the Au nanoparticles in more detail. The intensity increase in the peaks related to the polymer nanostructure as well as their constant position and asymmetry in q_y direction throughout the sputter-deposition is clearly visible. We fitted $I(q_y, q_z = 0.72 \pm 0.04$ nm^{-1}, $\delta)$ using Gauss−Voigt functions in order to extract quantitative growth kinetics, i.e., the radius and distance of the Au nanoparticles as well as the length scale of the phase-separated polymer structure during the sputter deposition. The height of the Au nanoparticles is extracted by using the procedure described in the Supporting Information. Figure 6

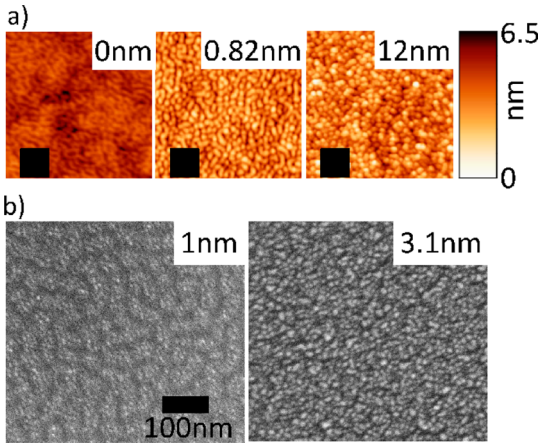

Figure 3. (a) Atomic force microscopy (AFM) image of the P(S-*b*-MMA) substrate, a nominal gold thickness of 0.82 nm and well beyond the percolation threshold (12 nm). The black square in each images represents an area of 200 nm x 200 nm. The color code presents the height in nm. (b) Field-emission scanning electron microscopy (FESEM) image of samples prepared at a nominal gold thickness of 1.6 and 3.1 nm. The AFM images clearly show the selective wetting of the PS-block during the gold sputter deposition before the percolation threshold is reached. The FESEM images clearly show that the gold nanoparticles grow on the PS domains.

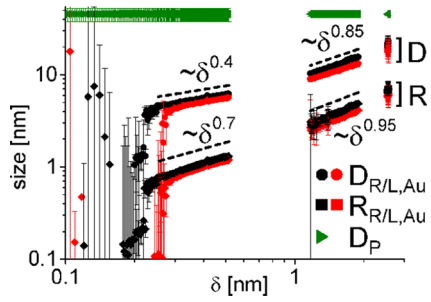

Figure 4. Evolution of the mean distance and radius of the Au nanoparticles as well as the (constant) domain size of PS in the PMMA-matrix. D_P denotes the domain size of the PS. Red symbols refer to the extracted values $q_y < 0$ nm^{-1} (denoted L), black symbols refer to the extracted values for $q_y > 0$ nm^{-1} (denoted R). The green symbols show the constant characteristic length scale of the PS-*b*-PMMA film. The dashed lines show different growth laws.[48]

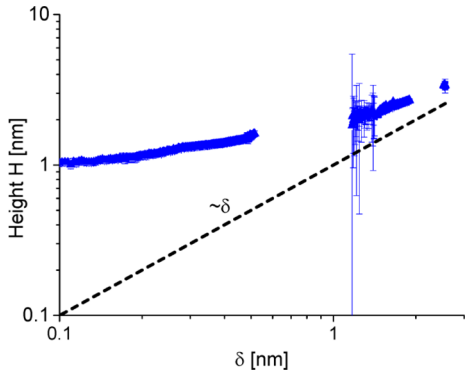

Figure 5. Evolution of the height of the nanoparticles. The dashed lines show the limit of 3D growth.

shows the intensity evolution of the polymer peak P situated at $q_y = -0.14$ nm^{-1}. Its intensity increases because of selective incorporation of Au on the PS block, then drops when the Au

DOI: 10.1021/am507727f
ACS Appl. Mater. Interfaces 2015, 7, 12470−12477

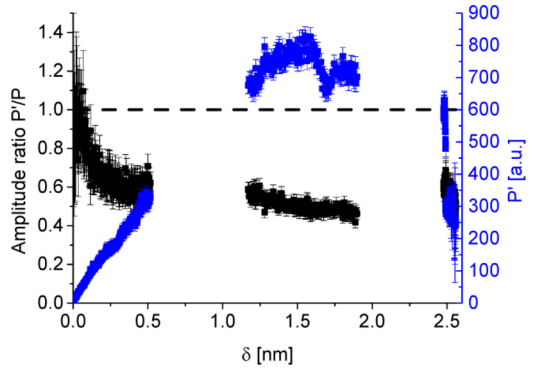

Figure 6. Evolution of the of the structure factor peaks P′ and P at $q_y = \pm 0.138$ nm^{-1}. The P′/P ratio initially decreases, then levels off around 0.5. The decrease from an initially symmetric value of 1 is due to the oblique angle deposition of Au. The dashed line shows the expected ratio for conventional incidence sputter deposition. The blue line shows the amplitude of the structure factor P in blue. The trend shows an increase of the amplitude due to selective coating of PS, at larger Au thicknesses the Au nanoparticle contribution dominates. This leads to a decrease when the Au deposition becomes less selective, when approaching the percolation threshold; also see AFM image $\delta = 12$ nm.

film thickness increases. The intensity ratio of the peaks denoted P′ and P in Figure 2 is a measure of the asymmetry of the peaks induced by GLAD. To the best of our knowledge, this effect has been observed for the first time in the present investigation. It is clearly seen that the ratio decreases rapidly up to $\delta = 0.1$ nm and then levels off at a constant value of 0.5. In normal incidence sputter deposition, such a behavior is not observed.[51,52]

Concerning the Au nanoparticles, the GISAXS pattern in Figure 1 and the line cuts in Figure 2 (N) clearly show the growth of these nanoparticles. The side maximum stems from the interparticle distance[15,51] and can be calculated using $D = 2\pi/q_0$, where q_0 denotes the position of the side maximum. Following the model of Schwartzkopf et al.,[51] we may assume a local hexagonal arrangement of nanoparticles. However, following Roth et al.,[59] we may assume a more cylindrical shape of the nanoparticles in the present case. By combining these two assumptions, we are able to calculate the mean radius of the particles R. To do so, we can express the radius R of the cylindrical nanoparticles as a function of δ, the height H of the nanoparticles, and q_0

$$R(D, \delta, H) = \sqrt{\frac{\sqrt{3}}{4\pi}\frac{D^2\delta}{H}} \quad (1)$$

H has been derived from the intensity distribution along the q_z direction, as described in the Supporting Information, and is shown in Figure 5. One immediately notes that the height of the nanoparticles grows in a nonlinear way because of self-assembly and the confinement to the PS block because of diffusion,[60] following a 3D growth mode.[49] Only in later stages ($\delta > 2$ nm) does the increase in height follow the standard linear law in thickness δ.[49] For $q_y < 0$ nm^{-1}, also denoted as left side L of the scattering pattern, and for $q_y > 0$ nm^{-1}, also denoted as right side R of the scattering pattern, the apparent distance of the Au nanoparticles differs, as can be seen from the fitting results in Figure 4. Using this finding in combination with eq 1, we obtain the different radii in Figure 4 for $q_y < 0$ nm^{-1} and $q_y > 0$ nm^{-1}. Please note that we obtain $R_L < R_R$, which is to be expected because of the growth in GLAD direction. At the same time, as seen in Figure 4, the position of the polymer signal stays constant.

We have incorporated different growth laws defining different growth regimes in D and R of the nanoparticles. Following Kaune et al.,[49] it has been found that $D, R \approx \delta^{\alpha}$ with α being an exponent $0 < \alpha < 1$. After the nucleation threshold around $\delta = 0.2$ nm, where significant lateral nanoparticle growth sets in, we obtain $\alpha_D = 0.4$ for the scaling factor of the distance and $\alpha_R = 0.7$ for the scaling factor of the radius. After the transition point around $\delta = 0.8$ nm, $\alpha_D = 0.85$, and $\alpha_R = 0.95$. It is important to note that the scaling law is the same for $q_y < 0$ nm^{-1} and $q_y > 0$ nm^{-1}.

3.1. Refined Model. In general, the three derived growth regimes are characterized by the predominant surface processes, namely (1) nucleation, (2) diffusion-mediated growth, and (3) adsorption mediated growth. They are basically comparable to the growth regimes observed from gold cluster growth on silicon substrates during normal incidence sputter deposition.[51] However, two important aspects need to be incorporated, which are equally important for tailoring hybrid materials. On the one hand, because of the oblique incidence of atoms during GLAD, the clusters tend to grow asymmetrically via direct adsorption from the gaseous phase. This is clearly illustrated using AFM, see $\delta = 120$ nm in Figure S5 in the Supporting Information. During the early stages of growth observed in the GISAXS experiment, the GLAD induced asymmetry of the nanoparticles manifests itself in two different radii of curvature for the nanoparticles, as we have already described above. This leads to the asymmetric GISAXS pattern with respect to the in-plane $q_y = 0$ nm^{-1} direction, very well pronounced for, e.g., $\delta = 1.56$ nm and $\delta = 2.56$ nm. On the other hand, it is important to note that the diffusion coefficients on both blocks of the diblock copolymer are quite distinct. Following Ruffino et al.,[60] Au shows a 64% increased surface diffusion on PS compared to PMMA. This may be attributed to the chemical nature of PMMA with its C−O bonds that would sequester the Au atoms, making them less mobile. On the other hand, the high mobility in the PS allows a faster metal atom diffusion and coalescence, which lead to large particles on the PS domains. This difference in mobility results in a different wetting behavior, which in turn affects the cluster growth kinetics. Therefore, taking into account the different Au−polymer interaction of PS and PMMA, the above-mentioned general growth stages can be refined.

1. Nucleation regime up to $\delta = 0.2$ nm: Initially, the Au atoms impinge on the surface and adsorb.[61,62] Because of the weaker polymer−gold interaction compared to the gold−gold interaction,[63,64] they diffuse as adatoms randomly on the surface. Upon impinging on each other, they may create a nucleus for a nanoparticle and eventually cluster. Because the adatom mobility is higher on PS, the chance of a seed-forming collision event is significantly increased. Thus, PMMA is more devoid of Au atoms than PS. This explains a preferred nucleation of Au on PS, which positively affects further cluster growth. Hence, the Au layer first reproduces the phase-separated morphology of the underlying substrate.[13,52,53] This explains the increase of intensity of the polymer characteristic peaks, see Figures 1 and 2. In normal incidence deposition, both peaks remain symmetric in intensity[52,53] However, the noticeable asymmetry for $q_y <$

DOI: 10.1021/am507727f
ACS Appl. Mater. Interfaces 2015, 7, 12470−12477

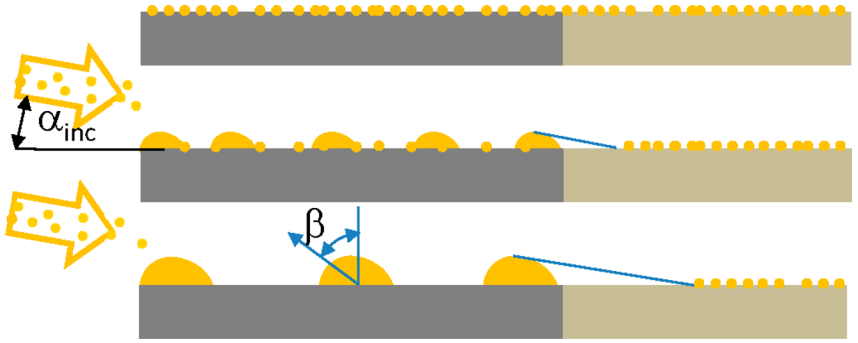

Figure 7. Model of the selective growth of Au on PS-*b*-PMMA. The GLAD angle α_{inc} is 10°. Top: Initially, the atoms impinge on the PS-*b*-PMMA surface. Dark gray denotes the PS domains, light gray the PMMA domains. Middle: Because of GLAD, anisotropic structures build up because of self-assembly. The growth direction follows an angle of $\beta = 55° \pm 3°$, because of shadowing effects as well as direct growth from adatoms. Bottom: Increase in the depletion region in the PMMA domains because of the shadowing effects.

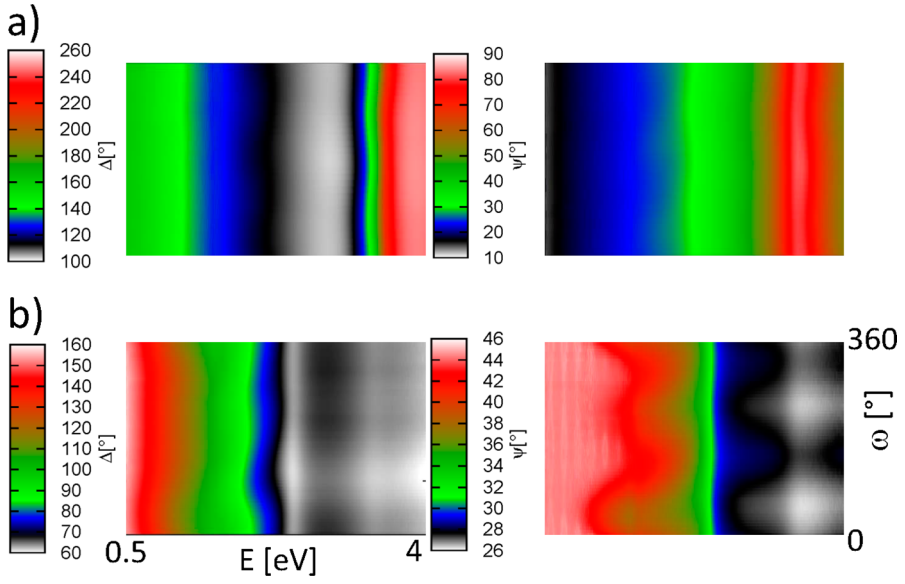

Figure 8. (a) Map of Δ and Ψ for $\delta = 0.82$ nm for an angle of incidence of 60°. $\omega = 0°$ corresponds to the *y*-direction, i.e., the direction of GLAD, see Figure S1 in the Supporting Information. (b) Map of Δ and Ψ for $\delta = 120$ nm for an angle of incidence of 70°. $\omega = 0°$ corresponds to the GLAD direction.

$0\ \text{nm}^{-1}$ and $q_y > 0\ \text{nm}^{-1}$ is already established after a very low $\delta \approx 0.1$ nm.

2. The diffusion-mediated growth up to $\delta = 0.9$ nm: Although nucleation is still present, the clusters themselves diffuse on the surface. Their diffusion is again governed by the different diffusion coefficients on both PS and PMMA domains.[65,66] The metal clusters may grow by capturing free adatoms from the surface as well as by propagating collisions of the metal clusters themselves. Hereby, the metal clusters coalesce to form a bigger metal cluster, and thus reduce their surface energy. Because of selective wetting of Au on PS, diffusion-mediated metal cluster growth via self-assembly on PS becomes more likely than on PMMA. Combined with the decrease in diffusion coefficient of Au from PS to PMMA, we may expect an increased concentration of Au at the domain boundaries. The consequence is 2-fold. First, the polymer structure factor peaks increase further with sputter time. Second, due to the shadowing, neighboring PMMA domains will show a depletion zone, where no new atoms can impinge directly, see Figure 7. The asymmetric concentration of Au atoms and metal clusters induced by the shadowing becomes enhanced, meaning that larger metal cluster on PS domains absorb more from atoms the gas phase and respectively fewer atoms can impinge on the PMMA. This shadowing and depletion zone might explain the asymmetry in the polymer structure factor. These phenomena may possibly be exploited in directional refractive index tuning.
3. Adsorption-driven growth from $\delta > 2$ nm: As the metal clusters size increase, the metal clusters become more and more immobile. At a critical radius of $R \approx 3$ nm, the metal clusters grow preferentially by attachment of atoms from the gas phase. During GLAD, especially at this low angle of incidence of 10°, anisotropic metal cluster growth and shadowing effects during deposition become important.[58] The latter might stem from surface roughness as well as from self-shadowing because of growing gold cluster structures. As indicated above, gold clusters first occur on PS domains and tend to grow faster in size. Because of the shadowing, the asymmetric concentration becomes enhanced, meaning that larger gold clusters on PS domains adsorb directly more atoms

DOI: 10.1021/am507727f
ACS Appl. Mater. Interfaces 2015, 7, 12470−12477

from the gaseous phase and tend grow faster in size, see Figure 7. During further deposition, the metal layer becomes coarsened, and the surface coverage further increases, while the depletion zone becomes reduced due to finite diffusion coefficients. At δ = 12 nm, a fully covered film is observed and the correlation of the Au layer to the substrate is lost, see Figure 3a.

The refined growth model is shown in Figure 7. First, atoms impinge on the PS-*b*-PMMA thin film. They diffuse to the PS domains, and nucleation preferentially occurs there, thus increasing the difference in electron density between the PS and the PMMA domains. Once clusters are established, the self-shadowing becomes important, leading on the one hand to the depletion zone in PMMA and on the other hand to the noncentrosymmetric nanoparticles. Finally, because of the diffusion of the Au atoms and the finite mobility of the Au clusters, also the PMMA domains, hitherto rather devoid of Au atoms compared to PS domains, become covered, and growth sets in there, too.

Additional measurements with spectroscopic ellipsometry confirm the asymmetry of the nanoparticles for two thicknesses δ = 0.82 and 120 nm. Figure 8a, b shows the corresponding maps of the ellipsometric parameters Δ and Ψ as a function of the light energy at an incident angle of 60° for the two Au thicknesses. Clearly, the observed anisotropic behavior in the 2−3.5 eV range stems from the slightly anisotropic nanoparticles.

At 3.6 eV, an oscillation is visible. This stems from an interference between the substrate and the polymer layer and leads to an oscillation in Δ and Ψ. In Figure 8b, Δ and Ψ values for δ = 120 nm are shown. The data show a broken 2-fold symmetry because of the polarizer position of 45°. The low-energy anisotropy corresponds to a change in the mean free carrier density interacting with the light. In the Supporting Information, additional maps are shown. Even for small thicknesses, the sputtered layer displays an anisotropic behavior parallel to the sample surface. For thick films, a clear Drude like term is visible in the Δ and Ψ values, and a broken 2-fold symmetry is observed.

This corroborates our model and at the same time shows novel perspectives for tailoring directional nanomaterials.

4. CONCLUSION

We combined oblique angle deposition of Au with a nanostructured diblock copolymer templates with different molecular weights. Our fundamental study shows a very simple route to create directional nanostructures via selective doping and self-assembly. Exploiting the strong Au−Au interaction and the differences in diffusion on both blocks as well as the phase-separated polymer morphology, we are able to obtain a hierarchical material. The spectral response is clearly asymmetric, as proven by spectroscopic ellipsometry. The asymmetry manifests itself in noncentrosymmetric nanoparticles on top of the PS domains. This new feature that we introduce here, directional nanostructures on selected domains only, is of great interest for applications in organic photovoltaics and electronics, which for example, may now be combined with directional optical coupling.[41]

■ ASSOCIATED CONTENT

Supporting Information

Overview over all morphological and structural parameters of the nanoparticles' growth (Figure S1). GISAXS geometry (Figure S2). Glancing angle deposition. Ex situ samples: UV−vis (Figures S3 and S4). AFM images (Figure S5). GLAD angle determination (Figures S6 and S7). Spectroscopic ellipsometry (Figures S8−S11). Gold on PS-*b*-PMMA, different molecular weight (Figure S12). This material is available free of charge via the Internet at http://pubs.acs.org.

■ AUTHOR INFORMATION

Corresponding Author

*E-mail: Stephan.roth@desy.de.

Present Address

#S.Y. is currently at Royal Institute of Technology (KTH), Teknikringen 56−58, SE-10044 Stockholm, Sweden

Notes

The authors declare no competing financial interest.

■ ACKNOWLEDGMENTS

We thank DFG for funding via grants RO 4638/1 and MU 1487/18. P.M.-B. and E.M. acknowledge financial support by TUM.solar in the frame of the Bavarian Collaborative Research Project "Solar technologies go Hybrid" (SolTec), the Green-Tech Initiative (Interface Science for Photovoltaics - ISPV) of the EuroTech Universities and the Nanosystems Initiative Munich (NIM). Y.Y. thanks the China Scholarship Council (CSC) for funding. S. Y. acknowledges the Knut och Alice Wallenberg foundation for the kind financial support. We acknowledge Lara Frenzel (DESY) for help in XRR data analysis and Calvin Brett (UHH, DESY) for the UV-Vis measurements. We thank Sarathlal Koyiloth Vayalil for help in the sample preparation.

■ REFERENCES

(1) Zhang, R.; Olin, H. Porous Gold Films—A Short Review on Recent Progress. *Materials* **2014**, *7*, 3834−3854.

(2) Kim, J.-H.; Bohra, M.; Singh, V.; Cassidy, C.; Sowwan, M. Smart Nanocomposite Sheets with Adaptive Optical Properties. *ACS Appl. Mater. Interfaces* **2014**, *6*, 13339−13343.

(3) Amarandei, G.; O'Dwyer, C.; Arshak, A.; Thiele, U.; Steiner, U.; Corcoran, D. Effect of Au Nanoparticle Spatial Distribution on the Stability of Thin Polymer Films. *Langmuir* **2013**, *29*, 6706−6714.

(4) Metwalli, E.; Krisch, I.; Markovits, I.; Rawolle, M.; Ruderer, M. A.; Guo, S.; Wyrzgol, S.; Jentys, A.; Perlich, J.; Lercher, J. A.; Müller-Buschbaum, P. Polymer Coated PtCo Nanoparticles Deposited on Diblock Copolymer Templates: Chemical Selectivity versus Topographical Effects. *ChemPhysChem* **2014**, *15*, 2236−2239.

(5) Kylian, O.; Petr, M.; Serov, A.; Solar, P.; Polonskyi, O.; Hanus, J.; Choukourov, A.; Biederman, H. Hydrophobic and Super-hydrophobic Coating Based on Nanoparticles Overcoated by Fluorocarbon Plasma Polymer. *Vacuum* **2014**, *100*, 57−60.

(6) Singh, J. P.; Chu, H. Y.; Abell, J.; Tripp, R. A.; Zhao, Y. Flexible and Mechanical Strain Resistant Large Area SERS Active Substrates. *Nanoscale* **2012**, *4*, 3410−3414.

(7) Amarandei, G.; O'Dwyer, C.; Arshak, A.; Corcoran, D. Fractal Patterning of Nanoparticles on Polymer Films and Their SERS Capabilities. *ACS Appl. Mater. Interfaces* **2013**, *5*, 8655−8662.

(8) Pfaff, M.; Müller, P.; Bockstaller, P.; Müller, E.; Subbiah, J.; Wing Ho Wong, W.; Klein, M. F. G.; Kiersnowski, A.; Reddy Puniredd, R. S.; Wojciech Pisula, W.; Colsmann, A.; Gerthsen, D.; Jones, D. J. Bulk Heterojunction Nanomorphology of Fluorenyl Hexa-perihexabenzo-

DOI: 10.1021/am507727f
ACS Appl. Mater. Interfaces 2015, 7, 12470−12477

coronene−Fullerene Blend Films. *ACS Appl. Mater. Interfaces* **2013**, *5*, 11554−11562.
(9) Schaffer, C. J.; Palumbiny, C. M.; Niedermeier, M. A.; Jendrzejewski, C.; Santoro, G.; Roth, S. V.; Müller-Buschbaum, P. A Direct Evidence of Morphological Degradation on a Nanometer Scale in Polymer Solar Cells. *Adv. Mater.* **2013**, *25*, 6760−6764.
(10) Lin, Y.; Böker, A.; He, J.; Sill, K.; Xiang, H.; Abetz, C.; Li, X.; Wang, J.; Emrick, T.; Long, S.; Wang, Q.; Balazs, A.; Russell, T. P. Self-directed Self-Assembly of Nanoparticle/Copolymer Mixtures. *Nature* **2005**, *434*, 55−59.
(11) Li, M.; Ober, C. K. Block Copolymer Patterns and Templates. *Mater. Today* **2006**, *9*, 30−39.
(12) Li, W.; Liu, M.; Qiu, F. Phase Diagram of Diblock Copolymers Confined in Thin Films. *J. Phys. Chem. B* **2013**, *117*, 5280−5288.
(13) Morkved, T. L.; Wiltzius, P.; Jaeger, H. M.; Grier, D. G.; Witten, T. A. Mesoscopic Self-Assembly of Gold Islands on Diblock-Copolymer Films. *Appl. Phys. Lett.* **1994**, *64*, 422−424.
(14) Abul-Kashem, M. M.; Kaune, G.; Diethert, A.; Wang, W.; Schlage, K.; Couet, S.; Röhlsberger, R.; Roth, S. V.; Müller-Buschbaum, P. Selective Doping of Block Copolymer Nanodomains by Sputter Seposition of Iron. *Macromolecules* **2011**, *44*, 1621−1627.
(15) Schlage, K.; Couet, S.; Roth, S. V.; Vainio, U.; Rüffer, R.; Abul Kashem, M. M.; Müller-Buschbaum, P.; Röhlsberger, R. The Formation and Magnetism of Iron Nanostructures on Ordered Polymer Templates. *New J. Phys.* **2012**, *14*, 043007.
(16) Dollinger, A.; Stolch, L.; Luo, Y.; Beck, M.; Strobel, C. H.; Hagner, M.; Dilger, S.; Bein, M.; Polarz, S.; Gantefoer, G. F.; Kim, Y. D.; Proch, S. Size-Selected Gold Clusters on Porous Titania as the Most "Gold-Efficient" Heterogeneous Catalysts. *Phys. Chem. Chem. Phys.* **2014**, *16*, 11017−11023.
(17) Al-Hussein, M.; Schindler, M.; Ruderer, M. A.; Perlich, J.; Schwartzkopf, M.; Herzog, G.; Heidmann, B.; Buffet, A.; Roth, S. V.; Müller-Buschbaum, P. In Situ X-ray Study of the Structural Evolution of Gold Nano-Domains by Spray Deposition on Thin Conductive P3HT Films. *Langmuir* **2013**, *29*, 2490−2497.
(18) Santoro, G.; Yu, S.; Schwartzkopf, M.; Zhang, P.; Koyiloth Vayalil, S.; Risch, J. F. H.; Rübhausen, M. A.; Hernandez, M.; Domingo, C.; Roth, S. V. Silver Substrates for Surface Enhanced Raman Scattering: Correlation between Nanostructure and Raman Scattering Enhancement. *Appl. Phys. Lett.* **2014**, *104*, 243107.
(19) Gill, R. S.; Saraf, R. F.; Kundu, S. Self-Assembly of Gold Nanoparticles on Poly(allylamine Hydrochloride) Nanofibre: A New Route to Fabricate "Necklace" as Single Electron Devices. *ACS Appl. Mater. Interfaces* **2013**, *5*, 9949−9956.
(20) Abdellah, A.; Virdi, K. S.; Meier, R.; Döblinger, M.; Müller-Buschbaum, P.; Scheu, C.; Lugli, P.; Scarpa, G. Successive Spray Deposition of P3HT/PCBM Organic Photoactive Layers: Material Composition and Device Characteristics. *Adv. Funct. Mater.* **2012**, *22*, 4078−4086.
(21) Maret, M.; Liscio, F.; Makarov, D.; Doisneau-Cottignies, B.; Ganss, F.; Missiaen, J.-M.; Albrecht, M. Growth Temperature Effect on the Structure of CoPt Islands on NaCl(001) Studied by Grazing-Incidence Small-Angle X-Ray Scattering. *J. Appl. Crystallogr.* **2014**, *47*, 102−109.
(22) Portale, G.; Sciortino, L.; Albonetti, C.; Giannici, F.; Martorana, A.; Bras, W.; Biscarini, F.; Longo, A. Influence of Metal−Support Interaction on the Surface Structure of Gold Nanoclusters Deposited on Native SiOx/Si Substrates. *Phys. Chem. Chem. Phys.* **2014**, *16*, 6649−6656.
(23) Han, Y.; Ferrando, R.; Li, Z. Y. Atomic Details of Interfacial Interaction in Gold Nanoparticles Supported on MgO(001). *J. Phys. Chem. Lett.* **2014**, *5*, 131−137.
(24) Krause, B.; Darma, S.; Kaufholz, M.; Gräfe, H.-H.; Ulrich, S.; Mantilla, M.; Weigel, R.; Rembold, S.; Baumbach, T. Modular Deposition Chamber for In Situ X-Ray Experiments During RF and DC Magnetron Sputtering. *J. Synchrotron Radiat.* **2012**, *19*, 216−222.
(25) Liang, L. Y.; Cao, H. T.; Liu, Q.; Jiang, K. M.; Liu, Z. M.; Zhuge, F.; Deng, F. L. Substrate Biasing Effect on the Physical Properties of Reactive RF-Magnetron-Sputtered Aluminum Oxide Dielectric Films on ITO Glasses. *ACS Appl. Mater. Interfaces* **2014**, *6*, 2255−2261.
(26) Nolte, P.; Stierle, A.; Jin-Phillipp, N. Y.; Kasper, N.; Schulli, T. U.; Dosch, H. Shape Changes of Supported Rh Nanoparticles During Oxidation and Reduction Cycles. *Science* **2008**, *321*, 1654−1658.
(27) Renaud, G.; Lazzari, R.; Rlevenant, C.; Barbier, A.; Noblet, M.; Ulrich, O.; Leroy, F.; Jupille, J.; Borensztein, Y.; Henry, C. R.; Deville, J.-P.; Scheurer, F.; Mane-Mane, J.; Fruchart, O. Real-Time Monitoring of Growing Nanoparticles. *Science* **2003**, *300*, 1416−1419.
(28) Green, I. X.; Tang, W.; Neurock, M.; Yates, J. T., Jr. Spectroscopic Observation of Dual Catalytic Sites During Oxidation of CO on a Au/TiO_2 Catalyst. *Science* **2011**, *333*, 736−739.
(29) Britnell, L.; Ribeiro, R. M.; Eckmann, A.; Jalil, R.; Belle, B. D.; Mishchenko, A.; Kim, Y.-J.; Gorbachev, R. V.; Georgiou, T.; Morozov, S. V.; Grigorenko, A. N.; Geim, A. K.; Casiraghi, C.; Castro Neto, H.; Novoselov, K. S. Strong Light-Matter Interactions in Heterostructures of Atomically Thin Films. *Science* **2013**, *340*, 1311−1314.
(30) Tian, C. G.; Jiang, D. Y.; Li, B. Z.; Lin, J. Q.; Zhao, Y. J.; Yuan, W. X.; Zhao, J. X.; Liang, Q. C.; Gao, S.; Hou, J. H.; Qin, J. Performance Enhancement of ZnO UV Photodetectors by Surface Plasmons. *ACS Appl. Mater. Interfaces* **2014**, *6*, 2162−2166.
(31) Polonskyi, O.; Kylian, O.; Drabik, M.; Kousal, J.; Solar, P.; Artemenko, A.; Cechvala, J.; Choukourov, A.; Slavinska, D.; Biederman, H. Deposition of Al Nanoparticles and their Nanocomposites Using a Gas Aggregation Cluster Source. *J. Mater. Sci.* **2014**, *49*, 3352−3360.
(32) Alvarez, R.; Garcia-Martin, J. M.; Macias-Montero, M.; Gonzalez-Garcia, L.; Gonzalez, J. C.; Rico, V.; Perlich, J.; Cotrino, J.; Gonzalez-Elipe, A. R.; Palmero, A. Growth Regimes of Porous Gold Thin Films Deposited by Magnetron Sputtering at Oblique Incidence: From Compact to Columnar Microstructures. *Nanotechnology* **2013**, *24*, 045604.
(33) González-García, L.; Barranco, A.; Muñoz Páez, A.; González-Elipe, A. R.; García-Gutiérrez, M.-C.; Hernández, J. J.; Rueda, D. R.; Ezquerra, T. A.; Babonneau, D. Structure of Glancing Incidence Deposited TiO_2 Thin Films as Revealed by Grazing Incidence Small-Angle X-ray Scattering. *ChemPhysChem* **2010**, *11*, 2205−2208.
(34) Camelio, S.; Babonneau, D.; Lantiat, D.; Simonot, L.; Pailloux, F. Anisotropic Optical Properties of Silver Nanoparticle Arrays on Rippled Dielectric Surfaces Produced by Low-Energy Ion Erosion. *Phys. Rev. B* **2009**, *80*, 155434.
(35) Patzig, C.; Karabacak, T.; Fuhrmann, B.; Rauschenbach, B. Glancing Angle Sputter Deposited Nanostructures on Rotating Substrates: Experiments and Simulations. *J. Appl. Phys.* **2008**, *104*, 094318.
(36) Hajireza, P.; Krause, K.; Brett, M.; Zemp, R. Glancing Angle Deposited Nanostructured Film Fabry-Perot Etalons for Optical Detection of Ultrasound. *Opt. Express* **2013**, *21*, 6391−6400.
(37) Wang, S.; Fu, X.; Xia, G.; Wang, J.; Shao, J.; Fan, Z. Structure and Optical Properties of ZnS Thin Films Grown by Glancing Angle Deposition. *Appl. Surf. Sci.* **2006**, *252*, 8734−8737.
(38) Mark, A. G.; Gibbs, J. G.; Tung-Chun Lee, T.-C.; Fischer, P. Hybrid Nanocolloids with Programmed Three-Dimensional Shape and Material Composition. *Nat. Mater.* **2013**, *12*, 802−807.
(39) Fu, J.; Zhao, Y. Au Nanoparticle Based Localized Surface Plasmon Resonance Substrates Fabricated by Dynamic Shadowing Growth. *Nanotechnology* **2010**, *21*, 175303.
(40) Pfeiffer, M.; Lindfors, K.; Atkinson, P.; Rastelli, A.; Schmidt, O. G.; Giessen, H.; Lippitz, M. Positioning Plasmonic Nanostructures on Single Quantum Emitters. *Phys. Status Soidi. B* **2012**, *249*, 678−686.
(41) Dregely, D.; Lindfors, K.; Lippitz, M.; Nader Engheta, N.; Michael Totzeck, M.; Giessen, H. Imaging and Steering an Optical Wireless Nanoantenna Link. *Nat. Commun.* **2014**, *5*, 4354.
(42) Thurn-Albrecht, T.; Schotter, J.; Kästle, G. A.; N. Emley, N.; Shibauchi, T.; Krusin-Elbaum, L.; Guarini, K.; Black, C. T.; Tuominen, M. T.; Russell, T. P. Ultrahigh-Density Nanowire Arrays Grown in Self-Assembled Diblock Copolymer Templates. *Science* **2000**, *290*, 2126−2129.

DOI: 10.1021/am507727f
ACS Appl. Mater. Interfaces 2015, 7, 12470−12477

(43) Singh, D. P.; J.P. Singh, J. P. Controlled Growth of Standing Ag Nanorod Arrays on Bare Si Substrate Using Glancing Angle Deposition for Self-Cleaning Applications. *Appl. Phys. A: Mater. Sci. Process.* **2014**, *114*, 1189−1193.
(44) Lee, J.-W.; Mayer-Gall, T.; Opwis, K.; Song, C. E.; Gutmann, J. S.; List, B. Organotextile Catalysis. *Science* **2013**, *341*, 1225−1229.
(45) Zhao, Y.; Sugunan, A.; Rihtnesberg, D. B.; Wang, Q.; Toprak, M. S.; Muhammed, M. Size-Tuneable Synthesis of Photoconducting Poly-(3-Hexylthiophene) Nanofibres and Nanocomposites. *Phys. Status Solidi C* **2012**, *9*, 1546−1550.
(46) Sugunan, A.; Guduru, V. K.; Uheida, A.; Muhammet, S.; Toprak, M. S.; Muhammed, M. Radially Oriented ZnO Nanowires on Flexible Poly-L-Lactide Nanofibers for Continuous-Flow Photocatalytic Water Purification. *J. Am. Ceram. Soc.* **2010**, *93*, 3740−3744.
(47) Müller-Buschbaum, P. Influence of Surface Cleaning on Dewetting of Thin Polystyrene Films. *Euro. Phys. J. E* **2003**, *12*, 443−448.
(48) Müller-Buschbaum, P. Grazing Incidence Small-Angle X-Ray Scattering: An Advanced Scattering Technique for the Investigation of Nanostructured Polymer Films. *Anal. Bioanal. Chem.* **2003**, *376*, 3−10.
(49) Kaune, G.; M. A. Ruderer, M. A.; Metwalli, E.; Wang, W.; Couet, S.; Schlage, K.; Röhlsberger, R.; Roth, S. V.; Müller-Buschbaum, P. In Situ GISAXS Study of Gold Film Growth on Conducting Polymer Films. *ACS Appl. Mater. Interfaces* **2009**, *1*, 353−360.
(50) Yu, S.; Santoro, G.; Sarkar, K.; Dicke, B.; Wessels, P.; Bommel, S.; Döhrmann, R.; Perlich, J.; Kuhlmann, M.; Metwalli, E.; Risch, J. F. H.; Schwartzkopf, M.; Drescher, M.; Müller-Buschbaum, P.; Roth, S. V. Formation of Al Nanostructures on Alq3: An In Situ Grazing Incidence Small Angle X-ray Scattering Study during Radio Frequency Sputter Deposition. *J. Phys. Chem. Lett.* **2013**, *4*, 3170−3175.
(51) Schwartzkopf, M.; Buffet, A.; Körstgens, V.; Metwalli, E.; Schlage, K.; Benecke, G.; Perlich, J.; Rawolle, M.; Rothkirch, A.; Heidmann, B.; Herzog, G.; Müller-Buschbaum, P.; Röhlsberger, R.; Gehrke, R.; Stribeck, N.; Roth, S. V. From Atoms to Layers: In Situ Gold Cluster Growth Kinetics During Sputter Deposition. *Nanoscale* **2013**, *5*, 5053−5062.
(52) Metwalli, E.; Körstgens, V.; Schlage, K.; Meier, R.; Kaune, G.; Buffet, A.; Couet, S.; Roth, S. V.; Röhlsberger, R.; Müller-Buschbaum, P. Cobalt Nanoparticles Growth on a Block Copolymer Thin Film: A Time-Resolved GISAXS Study. *Langmuir* **2013**, *29*, 6331−6340.
(53) Metwalli, E.; Couet, S.; Schlage, K.; Röhlsberger, R.; Körstgens, V.; Ruderer, M.; Wang, W.; Kaune, G.; Roth, S. V.; Müller-Buschbaum, P. In Situ GISAXS Investigation of Gold Sputtering onto a Polymer Template. *Langmuir* **2008**, *24*, 4265−4272.
(54) Zehner, R. W.; Lopes, W. A.; Morkved, T. L.; Jaeger, H.; Sita, L. R. Selective Decoration of a Phase-Separated Diblock Copolymer with Thiol-Passivated Gold Nanocrystals. *Langmuir* **1998**, *14*, 241−244.
(55) Gopinathan, A. Kinetic Self-Assembly of Metals on Copolymer Templates. *Phys. Rev. E* **2005**, *71*, 041601.
(56) Lopes, W. A.; Jaeger, H. M. Hierarchical Self-Assembly of Metal Nanostructures on Diblock Copolymer Scaffolds. *Nature* **2001**, *414*, 735−738.
(57) Döhrmann, R.; Botta, S.; Buffet, A.; Santoro, G.; Schlage, K.; Schwartzkopf, M.; Bommel, S.; Risch, J. F. H.; Mannweiler, R.; Brunner, S.; Metwalli, E.; Müller-Buschbaum, P.; Roth, S. V. A New Highly Automated Sputter Equipment for In Situ Investigation of Deposition Processes with Synchrotron Radiation. *Rev. Sci. Instrum.* **2013**, *84*, 043901.
(58) Hawkeye, M. M.; Brett, M. J. Glancing Angle Deposition: Fabrication, Properties, and Applications of Micro- and Nanostructured Thin Films. *J. Vac. Sci. Technol. A* **2007**, *25*, 1307−1335.
(59) Roth, S. V.; Walter, H.; Burghammer, M.; Riekel, C.; Lengeler, B.; Schroer, C.; Kuhlmann, M.; Walther, T.; Sehrbrock, A.; Domnick, R.; Müller-Buschbaum, P. Combinatorial Investigation of the Isolated Nanoparticle to Coalescent Layer Transition in a Gradient Sputtered Gold Nanoparticle Layer on top of Polystyrene. *Appl. Phys. Lett.* **2006**, *88*, 021910.
(60) Ruffino, F.; Torrisi, V.; Marletta, G.; Grimaldi, M. G. Growth Morphology of Nanoscale Sputter-Deposited Au Films on Amorphous Soft Polymeric Substrates. *Appl. Phys. A: Mater. Sci. Process.* **2011**, *103*, 939−949.
(61) Venables, J. A.; Spiller, G. D. T.; Hanbücken, M. Nucleation and Growth of Thin Films. *Rep. Prog. Phys.* **1984**, *47*, 399−458.
(62) Kukushkin, S. A.; Osipov, A. V. Thin-Film Condensation Processes. *Phys.-Usp.* **1998**, *41*, 983−1014.
(63) Lopez, G. P.; Biebuyck, H. A.; Frisbie, C. D.; Whitesides, G. M. Imaging of Features on Surfaces by Condensation Figures. *Science* **1993**, *260*, 647−649.
(64) Avramopoulos, A.; Papadopoulos, M. G.; Sadlej, A. J. Strong Interactions through the X···Au−Y Bridge: The Au Bond? *Chem. Phys. Lett.* **2003**, *370*, 765−769.
(65) Zaporojtchenko, V.; Behnke, K.; Thran, A.; Strunskus, T.; Faupel, F. Condensation Coefficients and Initial Stages of Growth for Noble Metals Deposited onto Chemically different polymer surfaces. *Appl. Surf. Sci.* **1999**, *144−145*, 355−359.
(66) Petrov, I.; Barna, P. B.; Hultman, L.; Greene, J. E. Microstructural Evolution during Film Growth. *J. Vac. Sci. Technol. A* **2003**, *21*, S117−S128.

DOI: 10.1021/am507727f
ACS Appl. Mater. Interfaces 2015, 7, 12470−12477